Attitude and Power Analysis of Two-Node, Multi-Tethered Coulomb Structures

Carl R. Seubert, Stephen Panosian, and Hanspeter Schaub
University of Colorado, Boulder, CO 80309

DOI: 10.2514/1.52185

Simulated Reprint from

Journal of Spacecraft and Rockets

Volume 48, Number 6, Nov.–Dec., 2011, Pages 1033–1045

A publication of the
American Institute of Aeronautics and Astronautics, Inc.
1801 Alexander Bell Drive, Suite 500
Reston, VA 22091

JOURNAL OF SPACECRAFT AND ROCKETS
Vol. 48, No. 6, Nov.–Dec., 2011

Attitude and Power Analysis of Two-Node, Multi-Tethered Coulomb Structures

Carl R. Seubert,* Stephen Panosian,† and Hanspeter Schaub‡
University of Colorado, Boulder, CO 80309

DOI: 10.2514/1.52185

The tethered Coulomb structure is a novel approach to generating a large deployable and reconfigurable, near-rigid space structure. This concept uses electrostatic forces to repel a three-dimensional formation of spacecraft nodes interconnected through fine, low-mass tethers. The tethered Coulomb structure rotational stiffness characteristics are quantified through numerical analysis of the tethered Coulomb structure node attitudes. With a two-node configuration the rejection of angular rotation disturbances up to 50 deg/min are computed. The maximum absolute angular deflection is reduced as much as 75% by using a triple-tether over a single-tether. Further, the triple-tether setup can provide full three-dimensional stiffness even for a two-node system. Variations in tethered Coulomb structure nodal parameters show that low inertia nodes with wide tether attachments significantly increase the rotational stiffness. With applications targeted for geosynchronous Earth orbit, results show that the differential gravity gradient forces have minimal affect on relative nodal attitudes. In addition, representative geosynchronous Earth orbit plasma conditions are modeled to demonstrate that plasma partial shielding has minimal effect on structure inflation under Coulomb forces. Charging a tethered Coulomb structure to negative potentials is advantageous in that only Watt levels of power are required to maintain quasi-rigid formations.

Nomenclature

$\boldsymbol{F}_c$	=	Coulomb force (N)
e_c	=	elementary charge (C)
I_{cc}	=	charge control current (A)
I_{net}	=	net plasma current (A)
J_{net}	=	net plasma current density (Am^{-2})
J_{0e}, J_{0i}	=	electron, ion saturation current density (Am^{-2})
J_{pe}	=	net photoelectron current density (Am^{-2})
J_{0pe}	=	photoelectron saturation current density (Am^{-2})
κ	=	Boltzmann constant (JK^{-1})
k_c	=	vacuum Coulomb constant (Nm^2C^{-2})
λ_D	=	Debye length (m)
m	=	node mass (kg)
m_e, m_i	=	electron, ion mass (kg)
n_e, n_i	=	electron, ion density (m^{-3})
P	=	charge emission power (W)
ϕ	=	multi-tether attachment half angle (rad)
ψ	=	multi-tether geometry (rad)
q	=	node charge (C)
Q	=	combined charge product (C^2)
$\boldsymbol{r}$	=	node separation vector (m)
ρ	=	node spherical radius (m)
T_e, T_i	=	electron, ion temperature (eV)
T_{pe}	=	photoelectron mean temperature (eV)
T_{Se}	=	secondary electron temperature (ev)
θ	=	multi-tether geometry (rad)
V	=	generic potential (V)
V_{sc}	=	node potential (V)
$\hat{r}_{ij}$	=	unit vector between node i and j

I. Introduction

Large space-based platforms on the order of hundreds of meters and more are sought for remote sensing, high resolution surveillance, radiometry, space telescopes, space situational awareness or power collection. Spacecraft formations and large space structures are two methods of achieving a large space-based platform. It is desirable to have a spacecraft platform with shape adjustable capabilities to accommodate changing mission requirements as well as operate for long durations.

A large platform can be launched as a rigid structure. However, its size and mass is limited by the capabilities of the available launch vehicles. On-orbit construction can increase the overall dimensions of a rigid structure such as has been done with the assembly of the international space station; however, such structures require human construction or advanced autonomous assembly techniques. The design of deployable spacecraft components is an active research area with few having been successfully implemented or tested in space.[1–4]

Along with the development of large space structure technologies, sophisticated applications and missions are emerging. One such mission is the Eyeglass concept that is intended to be used for Earth surveillance from Geosynchronous Earth Orbit (GEO). A 25-100 m aperture diffractive lens is to be deployed on orbit.[5,6]

Two proposed missions that intend to generate large kilometer size baselines are the proposed NASA Stellar Imager[7] and the Terrestrial Planet Finder.[8] Both of these concepts utilize a formation of free-flying spacecraft. Free-flying formations offer advantages such as variable baselines, system redundancy and fractionated and responsive architectures.[9] The PRISMA mission is designed specifically to demonstrate advanced autonomous formation flying techniques.[10] A challenge with free-flying craft is the complex relative dynamics, challenging relative motion sensing requirements, and the associated control strategies which can often require high propellant usage, and consequently shortened missions, to maintain an accurate formation.

Spacecraft formations can be operated with conventional chemical thrusters or electric propulsion where the fuel propellant mass, or electrical power requirements, must be taken into careful consideration. Further, for close proximity operations less than 100 meters, the thruster exhaust plume impingement issues must be taken into account.

Over the last decade, novel, essentially propellant-less relative motion control concepts consider using either Coulomb electrostatic interactions,[11,12] magnetic formation flying,[13] Lorentz forces[14] or flux-pinning.[15] In particular, the use of inter-spacecraft

*Graduate Research Assistant, Aerospace Engineering Sciences Department, AIAA student member, AAS student member
†Graduate Research Assistant, Aerospace Engineering Sciences Department, AIAA student member, AAS student member
‡Associate Professor, H. Joseph Smead Fellow, Aerospace Engineering Sciences Department, AIAA Associate Fellow, AAS member
Presented as Paper 2010–8130 at the AIAA/AAS Astrodynamics Specialists Conference, Toronto, Canada, Diego, CA, Aug 2–5, 2010.

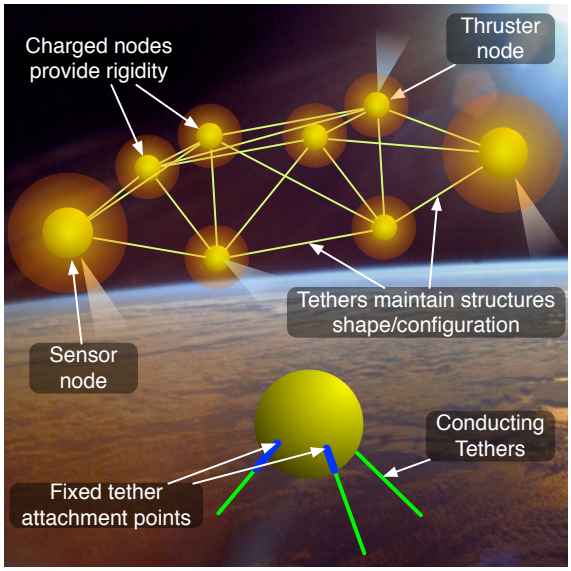

Figure 1: Tethered Coulomb Structure concept

Coulomb forces offers close formation relative motion control with low power and propellant requirements.[11,12,16] However, the control of a cluster of actively charged spacecraft remains a challenging research area due to the non-affine nature of the electrostatic force actuation. Analytically stable charge feedback control strategies are discussed for a two-spacecraft cluster in References 17–19, and for a three-vehicle cluster in Reference 20. The control of a larger formation with more than 3 vehicles remains an open research topic. Izzo and Pettazi propose the self-assembly of large space structures with Coulomb spacecraft.[21] However, their N-vehicle charge control law does not have analytical stability guarantees.

This paper investigates a recently introduced large space structure concept called the Tethered Coulomb Structure (TCS).[22,23] The TCS concept offers a number of advantages over the free-flying Coulomb spacecraft cluster concept in that the relative motion is constrained through the tether lengths. The TCS uses discrete spacecraft nodes that are inter-connected with fine, low-mass tethers as illustrated in Figure 1. Each node is repelled from the other TCS nodes through the use of electrostatic (Coulomb) forces. The inflationary Coulomb forces provide rigidity and shape control. The TCS size and shape is constrained by the tether lengths which limit how far the nodes can repel from each other. The electrostatic force is applied by manipulating each TCS node's potential with a charge control device. Here active emission of charged particles such as electrons or ions are used to drive the node potential away from its natural space weather dependent equilibrium to a desired potential level.

Similar to the Coulomb formation flying benefits, some key advantages of the TCS system is that it only requires Watt-levels of power and very little propellant (low mass ions or electrons). This provides the TCS with long term mission capabilities.[22] The main difference between TCS and Coulomb formation flying scenarios is that the charge control problem is significantly simplified. Instead of requiring precise charge levels to maintain relative positions, as well as complex non-affine control developments, the TCS only requires the charge levels to be maintained above a certain threshold that guarantees robustness to orbital perturbations. For example, to guarantee tether tension in the presence of differential gravity or solar radiation pressure, the electrostatic inflationary force must be larger than these perturbations.

TCS configuration sizes ranging from tens to hundreds of meters are envisioned by connecting strands of charged nodes with tethers. The TCS concept has the advantage of being launched in a compact and stored configuration, that is then inflated or deployed on-orbit. A key feature of TCS is that this Coulomb force inflation provides structural rigidity and an ability to resist deformation and disturbances. With length-adjustable tethers it is possible to change the structures shape and size on-orbit providing an adaptable nodal network to meet variable sensing and mission requirements. The concept can also be used to deploy and hold a small node in a fixed position from a primary spacecraft providing situational awareness or local sensing. An additional advantage of the TCS concept is that tether tensions can be maintained without requiring a particular orbit, equilibrium configuration or spin, like typical tethered systems.

Figure 2 shows how the concepts shape change attributes and control requirements compare to alternate space platform techniques. A large, monolithic space structure such as the Hubble space telescope is essentially launched and deployed as a single unit (except for the deployed solar arrays). This provides good overall rigidity with very little relative motion or flexing control requirements. Large space structure concepts are considered now. The iSat program for instance, envisions deployable structures that could reach 100 meters in size and larger. This increased shape changing ability results in a very light weight structure that might require active damping and smart materials to dampen out oscillations. Other large spacecraft concepts such as solar sails or gas-inflatable structures achieve even larger shape change capabilities with ever more light-weight structures. On the other end of large space platforms in Figure 2 are free-flying formations. Here the space platform shape is free to change subject to thruster propellant and power limitations. However, the relative motion sensing and control requirements are significantly increased in contrast to continuous structures such as iSat or solar sails. The proposed TCS concept falls between the current solar sail and inflatable concepts, and the free-flying spacecraft cluster concepts. While the TCS nodes are interconnected, the milli-Newton tether tensions are small enough such that the orbital motion must be taking into account when studying TCS dynamics.

Due to possible charge shielding from the local plasma environment it is necessary to operate a TCS at GEO altitudes or higher where the plasma is nominally hot and sparse. At GEO, a spacecraft can naturally charge to kilovolt potentials during periods of Earth eclipse. Such kilovolt charge levels are similar to the levels of charge that are considered for the TCS concept in this paper.[24,25] This charge can be controlled with charge emission technology that is already space-proven. One example is the volt-level control the European CLUSTER mission demonstrates.[26–28] A charge emission device can be used on each of the TCS nodes or on a single node and distributed to other nodes via conducting tethers. The benefits and draw backs of either scenario are being investigated.

The combination of both Coulomb forces and tethers is a unique and promising large space structure concept. The intent of this paper is to investigate the dynamic coupling and resulting rotational stiffness of tethered spacecraft that are inflated with electrostatics. Of interest is the ability of the TCS to bound angular rotations without the use of control or damping. This resulting worst-case operating scenario allows analysis of fundamental motions and their primary frequencies. The electrostatic forces and nodal tether arrangements must be such that sufficient restoring torques are produced that avoid a node rotating to a point where tethers become entangled with the craft. The nodes feature a symmetric mass moment of inertia for this study to isolate the effectiveness of these restoring torques. Future studies will investigate asymmetric mass moments of inertia and additional torque sources such as Coulomb forces for non-spherical craft.

Previous studies on the TCS concept analyze only relative motions without nodal attitudes,[22] or focus on simplified two-dimensional (2D) motions.[23] This paper expands upon these studies to quantify the three-dimensional (3D) rotational stiffness about all axes and angular rate disturbance rejection. This rotational motion feasibility is under investigation as it is more challenging to overcome than translational motions.[23] This is a vital step for the TCS development as a large-scale deployable space structure, or as a network of small sensor nodes for use in high Earth orbit.

In this paper a 3D dynamic TCS model is developed and used to explore rotational motions. A benchmark two-node system is presented to gain insight into the charge dependent TCS rigidity. This study investigates the feasible initial nodal rotation operating envelope including rotational stiffness sensitivity with respect

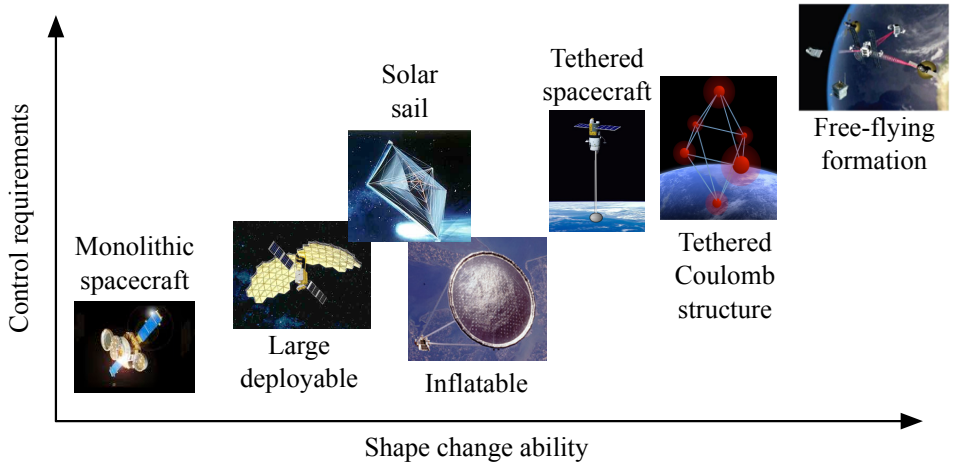

Figure 2: TCS concept shape change attributes and control requirements comparison

to the number of connecting tethers, spacecraft size, symmetric inertia properties, and local plasma shielding. The simulation is performed in deep space to isolate the analyzed motions from gravity forces. It is demonstrated that this is appropriate as the gravity force effects are negligible for the closely operating two-node system at GEO. In addition to the dynamic aspects, the TCS power required to maintain a fixed potential and overcome the net current from the plasma environment is computed.

II. Dynamic Model

This research utilizes a nonlinear numerical simulation that models a general number of spacecraft nodes that are tethered in a selectable configuration. Relative motion and attitude simulations are performed in the absence of gravity to examine system variation effects on charged nodal motions and determine the conditions that lead to tether entanglement with the TCS nodes, an undesired state.

A. Coulomb Force

A Coulomb force is generated from the electrostatic interaction of two charged bodies. In a vacuum the force magnitude between two bodies of charges q_1 and q_2 is computed as:

$$|\boldsymbol{F}_c| = k_c \frac{|q_1 q_2|}{r^2} \tag{1}$$

where $k_c = 8.99 \times 10^9\ \mathrm{Nm^2C^{-2}}$ is the vacuum Coulomb constant and r is the separation distance between the bodies. Assuming the body is a spacecraft comprised of an outer spherical surface maintaining a constant charge q_1, then the resulting potential in a vacuum is expressed as:

$$V_{sc1} = \frac{q_1 k_c}{\rho} \tag{2}$$

where ρ is the radius of the spherical craft.

In space, the Coulomb force is reduced (partially shielded) by free-flying charged particles of the local plasma environment. The strength of this shielding is parametrized by the Debye length λ_D.[29] Assuming a small craft potential compared to the local plasma thermal energy

$$e_c V_{sc1} \ll \kappa T_e$$

where $e_c = 1.602176 \times 10^{-19}$ C is the elementary charge, $\kappa = 1.38065 \times 10^{-23}\ \mathrm{JK^{-1}}$ is the Boltzmann constant and T_e is the plasma electron temperature in Kelvin, the potential about this charged craft is represented by the Debye-Hückel equation:[30,31]

$$V = k_c \frac{q_1}{r} e^{-(r-\rho)/\lambda_D} \tag{3}$$

This potential equation is used in this TCS simulation as it incorporates plasma shielding and resembles a conservative bound of the charge interaction the nodes will experience.[32] At GEO, the $e_c V_{sc1} \ll \kappa T_e$ condition is no longer true if the spacecraft charges to 1-10 kV potentials. As discussed in Reference 32, the neglected higher order terms of Poisson's partial differential equation, which led to Eq. (3), results in less plasma shielding of the electrostatic fields. Thus, the use of Eq. (3) is considered a conservative estimate of the actual potential that might exist about a body. The benefit of using Eq. (3) is that it allows for simplified analysis, and faster numerical simulations. Solving the full Poisson-Vlasov equations requires solving complex partial differential field equations.

Taking the gradient of the potential in Eq. (3) (assuming spherical symmetry) yields the resulting Coulomb force $\boldsymbol{F}_c$ relationship between charged craft 1 and 2:

$$\boldsymbol{F}_c = k_c \frac{q_1 q_2}{r_{12}^2} e^{-r_{12}/\lambda_D} \left(1 + \frac{r_{12}}{\lambda_D}\right) \hat{r}_{12} \tag{4}$$

The Debye length is based on the temperature and density of the local plasma. At GEO the plasma has Debye lengths ranging from 4–1000 m with a nominal value of approximately 200 m.[11,22] Debye lengths of this scale allow the use of Coulomb repulsion when operating with spacecraft separations of dozens of meters at GEO. Equations 1 and 4 bound the possible range of TCS inflationary force. As an example, two craft separated by 5 meters in a worst-case plasma ($\lambda_D = 4$ m) will experience a force reduction of 35.5%, using Equation 4 and only 0.03% in a nominal plasma ($\lambda_D = 200$ m). In general, TCS nodes charged to tens of kilovolts at GEO will violate ($e_c V_{sc1} \ll \kappa T_e$) and will therefore lie in between the range of these analytic forces. One method of obtaining a representative force level is by computing an effective Debye length that is based on plasma conditions and craft size and potential as demonstrated in Reference 32. The effective Debye length for the GEO TCS applications will typically be a factor of two to three times larger than the background plasma Debye length. Consequently this larger effective Debye length significantly reduces the plasma shielding on the Coulomb force for these higher spacecraft potentials. For consistency, this study uses the conservative and analytic Coulomb force of Equation 4.

This paper studies the use of spacecraft charging for generating and applying these Coulomb forces and the knowledge gained benefits concepts beyond TCS. Analysis of natural and induced charging in the presence of plasma interactions assists with the development of light weight space structures and inflatable components. These spacecraft concepts can be highly susceptible to spacecraft charging levels.

B. Three Dimensional Simulation

The Appendix outlines the full 3D nonlinear equations of motion that accommodate general TCS spacecraft configurations. The numerical TCS model allows analysis of the capabilities and operating regimes of the TCS along with a study of its dynamic behavior under realistic disturbance environments. Both the TCS node position and orientation are tracked individually subject to

orbital, rigid body dynamics and perturbations. The algorithm can perform TCS relative motion studies accommodating any number of nodes and tethers in any initial deep space or orbit configuration and includes inertial or relative disturbance forces. An example three-node TCS along with axis and tether definitions is shown in Figure 3.

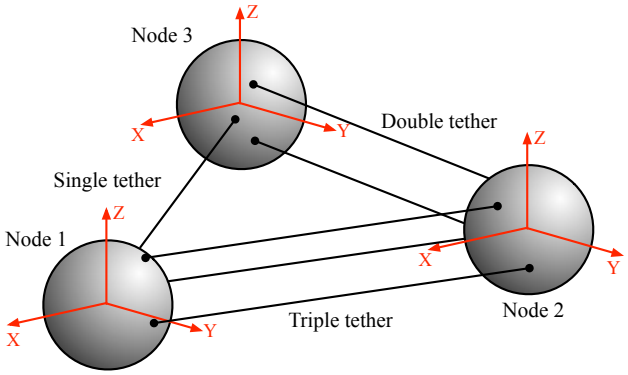

Figure 3: Dynamic model setup for a 3D three-node example

Each node can be connected with a single-tether or multiple tethers, but it is not necessary to have a tether connecting each node. The tether is modeled as a proportional spring. This allows for general tether stretching due to arbitrary nonlinear node translation and rotation. The tethers apply a force only for extensions from nominal length. When the tether length is shorter than desired, the tether goes slack and there is no tether force acting on the corresponding nodes. The inclusion of damping is beyond the scope of this paper and not included. Any future use of dissipative materials would result in small amounts of damping.

The use of a proportional spring tether model is justified through comparison of specific results to a high fidelity simulation using a finite element tether model. The University of Colorado developed code FEMDOC (Finite Element Multi-Disciplinary Optimization Code) uses a discrete tether model incorporating tether mass, deflections and buckling (tether diameter, material and thermal properties are currently under investigation). The differences in nodal motion results between FEMDOC and the model of this paper is less than 1 % as the tethers are very light (few grams) versus the TCS nodes (50 kg). Therefore, for the parameters used in this study, the proportional spring model is well suited for the rotational studies. However, if much lower mass nodes are used, or residual strain from thermal or tether material effects are included, the use of this model will have to be investigated further. Additionally, to verify the validity of the numerical simulation, the numerical TCS nodal translational and rotational motions for a single-tether configuration are compared to linearized approximations developed in Reference 23 and yield good agreement.

C. TCS Two-Node Simulation Parameters

A two-node TCS configuration in deep space is employed as a benchmark for analysis. A two-node configuration is chosen because it represents the lower bound of rotational stiffness for a TCS configuration. Furthermore, it allows focused examination of the effects of varying specific system parameters on rotational motions and tether entanglement. Specifically for this study, a two-node TCS configuration allows for rotational motion analysis using multiple tethers. Figure 4 shows the 3D, two-node configuration with a single- and double-tether connection as well as nodal forces.

Reference 23 explores the two-node system with asymmetric node rotations about the X-axis for configurations with one tether and provides preliminary results for systems with two tethers connecting two-nodes. Unlike this previous study that focused on specific 2D motions that allowed linearized analytic insight, only numerical studies are considered here due to the expanded 3D and highly nonlinear motions. This work expands upon this earlier work by examining asymmetric node rotations about all three axes for a single-, double- and triple-tether TCS configuration. Configurations with more than three tethers between two-nodes may

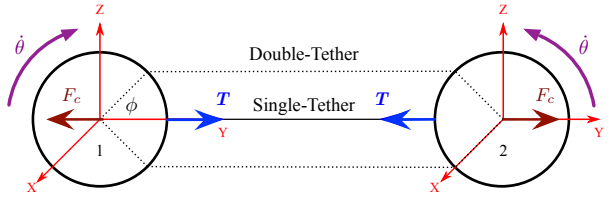

Figure 4: Two-node configuration showing single- and double-tether connections

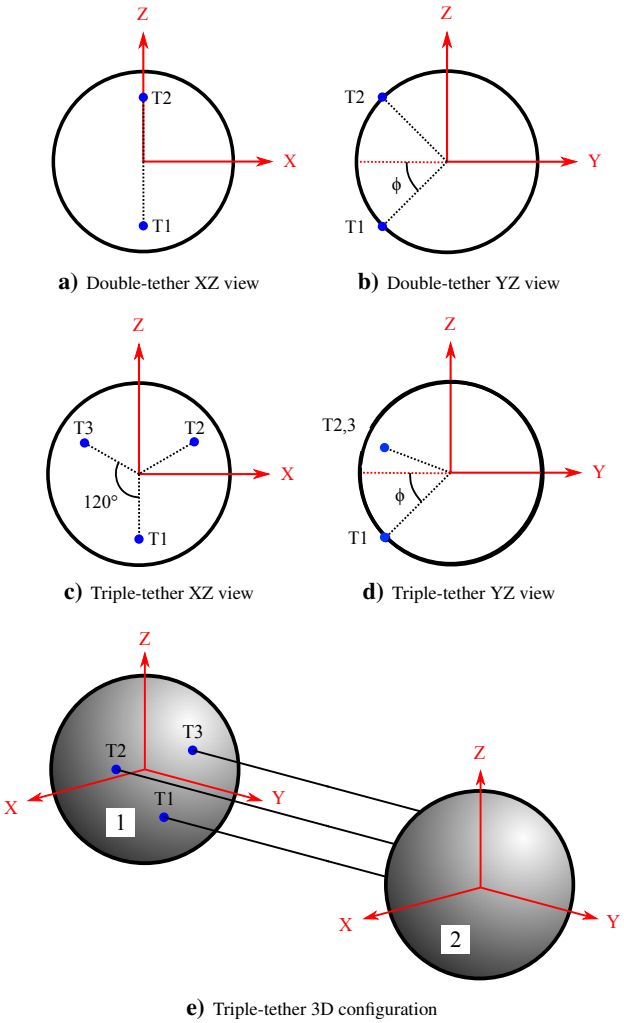

Figure 5: Two-node TCS tether configurations and connections

provide additional rotational stiffness. However, such configurations are not included in this study because the tether force solution is statically indeterminate and beyond the scope of this paper. The TCS two-node configuration with coordinate system and tether attachment points are illustrated in Figure 5.

Unless otherwise specified, the simulations are performed using the default parameter values given in Table 1. A separation distance of 5 meters is used as it is a practical nodal separation providing a suitable rotational stiffness as shown in previous work.[23] Lower separation distances provide increased stiffness, while 10 meters is toward the limit of nodal separations for suitable rotational stiffness with feasible charge levels. A default node mass of 50 kg and radius of 0.5 meters is chosen to coincide with previous work.[23] Additionally, these values are an approximate spacecraft size that is envisioned for a TCS and are appropriate for this feasibility study.

The tether spring constant is a representative value that is suitable for the simulations performed here. The chosen value is similar to that of AmberStrand®, which is a low mass conducting tether. Numerical simulations in Reference 23 show that the

Table 1: Default simulation parameters

Parameter	Value
Separation distance	5 m
Node mass	50 kg
Spring constant	3 N/m
Node charge	30 kV
Node radius	0.5 m
Initial angular rate	10 deg/min
Inertia distribution	Solid Sphere
Attachment angle ϕ	45 deg

tether spring constant has minimal effect on the rotational stiffness. Finally, a node charge of 30 kV is chosen because it is near natural charge levels and can be achieved with current charge emission devices.

At the start of the simulations, the nodes are aligned and the tethers are stretched to be in equilibrium with the repulsive Coulomb force. The disturbance modeled is an initial angular velocity applied to each of the two-nodes in an asymmetric method. Each node has an equivalent angular rate about a single axis but in opposite directions as shown in Figure 4. Although the initial disturbance is applied about a single axis, the coupling with multi-tether systems can cause arbitrary nodal rotations. For this reason the principal rotation vector magnitude is used to compare nodal responses.

Asymmetric rotation is chosen such that there is no net angular momentum in the two-node system. Studying the effect of initial angular velocities allows for various TCS configurations to be examined and determine if the tethered nodes reach an undesirable state. A node is considered entangled when the tether is tangent to the spheres surface at its attachment point, which could lead to wrapping up or for the multiple tether case, when the tethers make contact with each other. If spherical nodes with tethers attached on the surface are assumed, TCS configurations with various tether numbers and geometries will become entangled after different amounts of angular deflections.

The variation in entanglement angles can be seen for the single- and double-tether TCS configurations in Figure 4. Table 2 lists the nodal rotation angles at which each TCS configuration will reach the entangled state. The entanglement rotations in Table 2 are based upon geometry, where $\theta = \tan^{-1}(2\cot\phi)$ and $\psi = \tan^{-1}\left(2\cot\phi/\sqrt{3}\right)$. However, nodes are not likely to be spherical and the tether attachment points could be attached away from the nodes on booms, increasing the absolute rotations possible.

III. Rotational Stiffness Results

The primary emphasis of this study is the examination of the rotational motion of a two-node TCS configuration. The intent is to quantify the extent of rotational motion due to ranges of initial rotation rates and determine if the tether(s) will become entangled by wrapping up around the nodes. The resulting rotational dynamics provide an indication of the system rotational stiffness attributed to the tether and Coulomb force combination. The benchmark two-node configuration is used to examine the effect of several TCS parameters to perform a fundamental feasibility study.

A. Nodal Motion

A single-tether connection yields the simplest and most intuitive dynamics for a two-node TCS configuration under the disturbance of an initial angular velocity. Figure 6(a) shows the resulting dynamics of the single-tether system under an initial asymmetric nodal rotation about the X-axis. It is important to note that for all results the translational motion is only due to the rotational coupling, as the node is initially at translational equilibrium. Figure 6(a) shows the smooth and sinusoidal nodal separation, the asymmetric nodal rotations and the tether tension of a single-tether TCS. Under this small initial rotation disturbance (10 deg/min) the nodes rotate a maximum of 18 degrees about the X-axis and the tether remains under tension at all times. Larger initial disturbances can make the single-tether configuration go slack and cause the motion to no longer be sinusoidal. In contrast to the single-tether configuration, Figure 6(b) shows the translational and rotational motion for the double-tether configuration with initial rotations about the X-axis. The nodal motion is now piecewise linear. The nodes rotate, only about the X-axis, at a constant rate until the tethers become taut and reverse the direction of rotation. The piecewise linearity of a multiple tether TCS is due to the tethers no longer remaining continuously taut. This is shown by the plot of tether tension for each tether (T1 and T2). Maintaining a taut tether is not a required dynamic property, although there is concern of a tether reaching a buckled or tangled state. In these simulations each tether only reaches a slightly loose state on the order of millimeters over its entire 4 meter length.

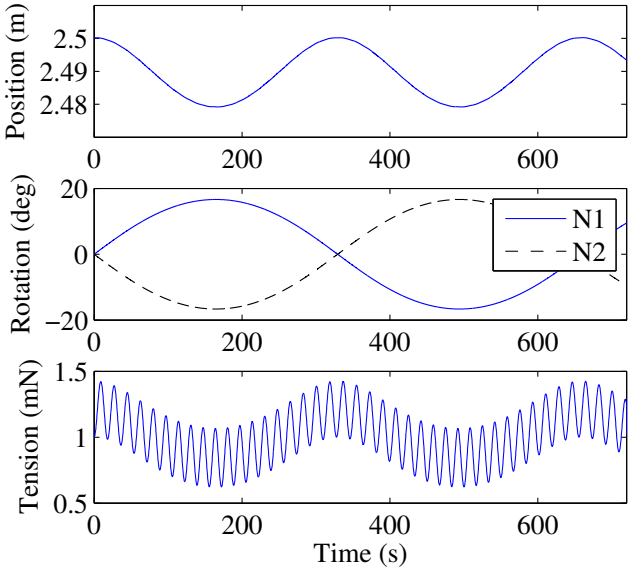

a) Single-tether configuration

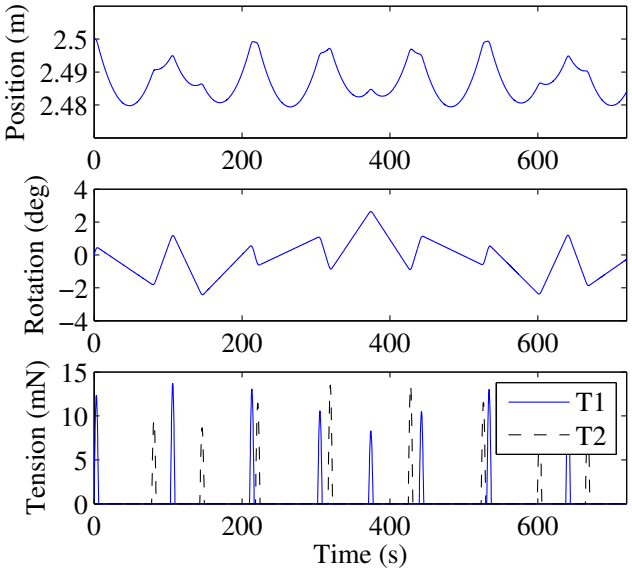

b) Double-tether configuration

Figure 6: TCS nodal dynamic response to asymmetric nodal rotation about the X-axis

The triple-tether configuration results for this X-axis rotation results in similar dynamics to that shown for the double-tether in Figure 6(b). Although the triple-tether demonstrates similar separations and X-axis rotations to the double-tether it adds another unique complexity to the two-node TCS configuration. The 3D spread of the triple-tether attachment points adds coupled off-axis rotational motions that is most apparent with rotations about the Z-axis. Figure 7 shows the three axes rotational motion of a triple-tether node with an initial rotation about the Z-axis. From the figure

Table 2: Spherical node rotation causing tether entanglement (for single-axis, asymmetric rotations)

Rotation Axis	Single-Tether (deg)	Double-Tether (deg)	Triple-Tether (deg)
X-axis (Node 1 Positive)	90	90 - ϕ	90 - θ
X-axis (Node 1 Negative)	90	90 - ϕ	90 - ϕ
Y-axis	N/A	90	90
Z-axis	90	90	90 - ψ

it can be seen that there is no longer pure rotation about the Z-axis. Figures 5(c) and 5(d) highlight the cause, showing that the connections for tethers 2 and 3 are no longer on a nodal axis and rotation leads to tether force moments and off-axis rotations. Figure 7(b) shows the resulting tensions for each tether, reiterating the coupling effect and piecewise motions.

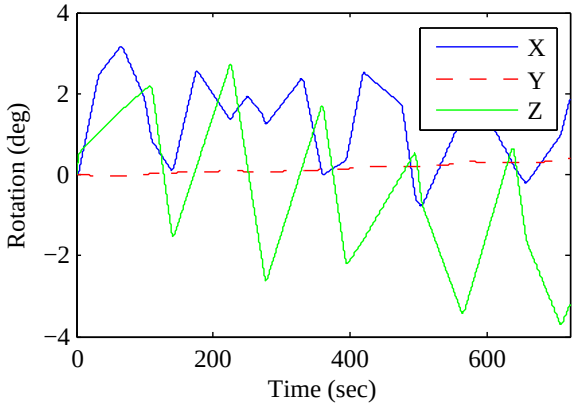

a) Three axes rotations

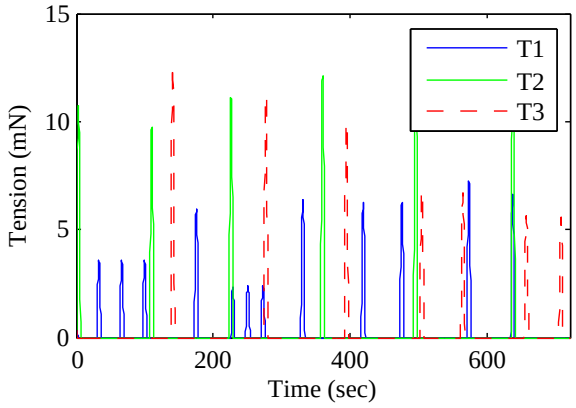

b) Tether tensions

Figure 7: Triple-tether nodal dynamic response to asymmetric nodal rotation about the Z-axis

B. Differential Gravity Effects at GEO

The previous section outlines the basic dynamics of a two-node TCS with no gravitational forces. However, TCS systems are envisioned to be operated at GEO where differential gravity can affect the nodal dynamics. The benchmark two-node TCS system is stable on orbit if the two-nodes are in an orbit radial configuration. Table 3 shows the percent difference between the maximum principal rotations of a two-node TCS system in deep space as compared to GEO. This is computed over a 12 hour simulation. For this benchmark two-node system it is evident that differential GEO forces have minimal effect on the rotation of the TCS nodes, with a maximum difference value of 2.24%. Therefore, differential gravity will be excluded from the remaining simulations so that the natural TCS system dynamics are isolated and analyzed. In addition, it is important to note that with differential gravity effects, rotations are no longer purely about a single axis for single- and double-tether TCS but they are very small respectively.

Table 3: Percentage difference of maximum principal rotation with GEO differential gravity forces [12 hr simulation]

Initial Rotation Axis	Single-tether	Double-tether	Triple-tether
X-Axis	-0.0839	0.6780	-1.1596
Y-Axis	N/A	-0.1514	-0.1514
Z-Axis	1.5793	1.3376	-2.2354

C. Multiple Tether Advantages

As shown in the prior sections, additional tethers between the two-node configuration adds complexity to the nodal dynamics. However, there are rotational stiffness advantages that multiple tethers provides. With the inability of a tether to hold torsional loads there is no stiffness in the Y-axis (for a single-tether) and only restoring torques for rotations about the X and Z axes are feasible. Using a TCS configuration with two or three tethers provides a restoring torque for rotations about any axis.

Additional tethers not only provide added system robustness to initial rotations, but they also reduce the maximum deflection a node can incur. The maximum angular deflection of the node is a measure of the TCS configuration rotational stiffness to an angular rate disturbance. Figure 8 demonstrates this by showing the maximum principal rotation angle reached as a function of initial angular rate. The maximum rotation is shown for each of the tether number configurations and shown for three cases; each with an initial rotation about a different axis. Note the difference in the angular rate axis of each of these figures. Angular rates about the Y-axis result in large rotations much faster than the other two axis rotations. It is shown in Table 2 that the multiple tether nodes have a reduced absolute rotation before entanglement occurs. For this reason Figure 9 shows the maximum rotation of the nodes relative to their corresponding entanglement rotation angle. Additionally, Figure 10 reiterates the effect of multiple tethers on node rotation by showing the absolute maximum rotations as a function of node potential. The rotation about each axis is analyzed using the results of Figures 8-10.

Case 1: Figure 8(a) shows that for asymmetric rotation about the X-axis, the addition of tethers reduces the maximum absolute angle reached from the single-tether case. For lower initial rotation rates, a double- and triple-tether configuration yield similar rotations. However, for rates above 30 deg/min a double-tether configuration provides more stiffness than a triple-tether configuration. This is likely due to the moment arms provided by the tethers. From Figures 5(b) and 5(d) it can be seen that the attachment points in the positive Z direction for the two tether configuration are further away from the X-axis than the three tether configuration. This difference provides a larger moment arm for the restoring torques and is one reason the double-tether configuration is stiffer at higher rates for this rotation. Additionally at higher rotation rates, the rotation coupling becomes more dominant which increases the maximum rotation rate for a three tether configuration.

While the addition of tethers certainly reduces the absolute rotational deflection of the node, the increased tether attachment locations places the node closer to the entanglement rotation. This is demonstrated in Figure 9(a) which shows the maximum angular

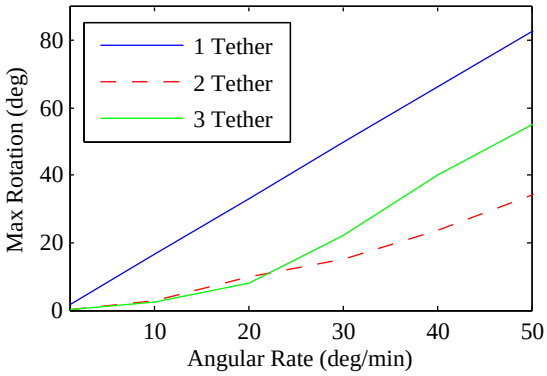

a) Case 1: X-axis rotation

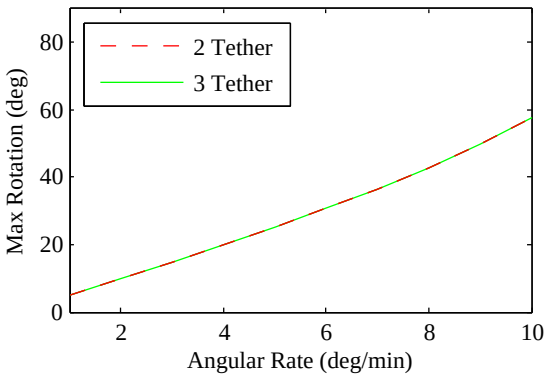

b) Case 2: Y-axis rotation

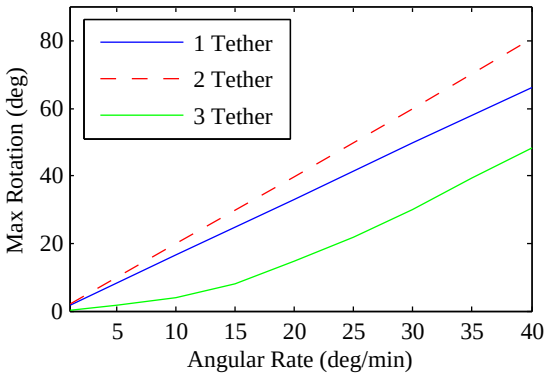

c) Case 3: Z-axis rotation

Figure 8: Maximum absolute principal rotation as a function of initial initial angular rate

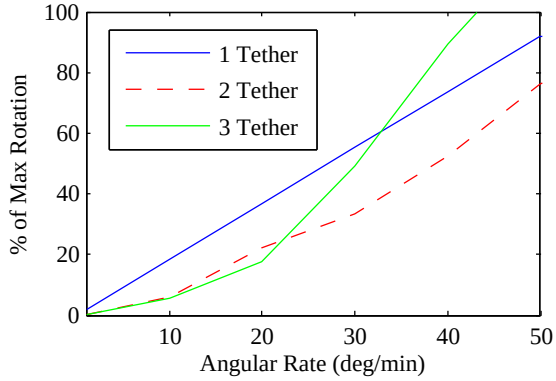

a) Case 1: X-axis rotation

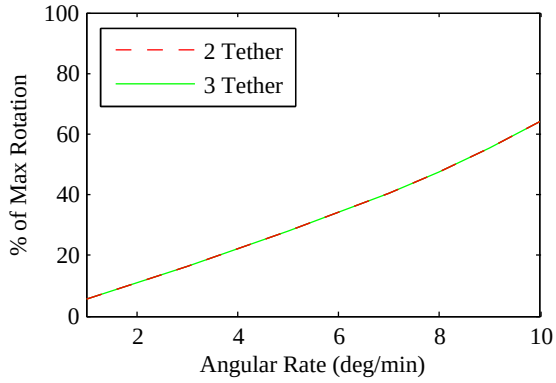

b) Case 2: Y-axis rotation

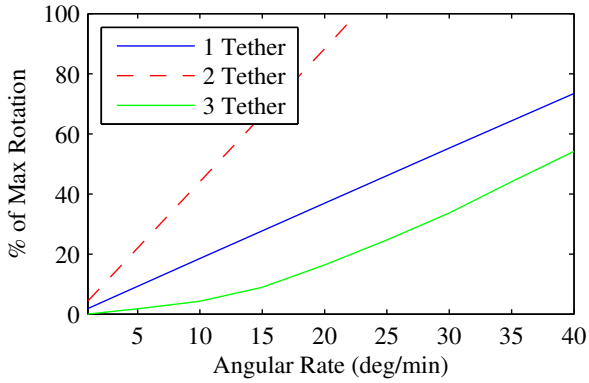

c) Case 3: Z-axis rotation

Figure 9: Maximum principal rotation relative to maximum entanglement rotation (Table 2)

deflection as a percentage of the entanglement rotation, which is a function of each tether configuration and rotation axis (as defined in Table 2). The result is that each tether configuration has a similar proximity to entanglement. The double-tether keeps the node further from entanglement than the single-tether, while the triple-tether results in entanglement with disturbances above 43 deg/min.

The effect of multiple tethers on X-axis rotation as a function of node potential is seen in Figure 10(a). The double- and triple-tether both provide more rotational stiffness across all node potentials than a single-tether TCS configuration. The double-tether does provide a slightly more stiff system than the triple-tether configuration. The non-smooth nature of the triple-tether configuration is due to the complex dynamics of the system, but a general exponential decay can still be seen.

Case 2: Rotational stiffness about the Y-axis for a double- and triple-tether configuration is shown in Figure 8(b). The single-tether configuration is omitted because it has no rotational stiffness for Y-axis rotations. From the Figure it can be seen that the double- and triple-tether configurations provide equal rotational stiffness about the Y-axis, because the moment arms about the Y-axis are equal. Figures 5(a) and 5(c) show how the moment arms are all the same radial distance from the Y-axis.

Figure 9(b) shows how close the Y-axis angular deflection comes to reaching the entanglement angle. The Y-axis has a reduced disturbance angular rate as the nodes have less rotational stiffness, however the inclusion of additional tethers provides prevention of entanglement for the disturbance range analyzed. In this case the single-tether entanglement rotation is undefined as the tether is bound about itself.

Figure 10(b) provides additional evidence of the effects of multiple tethers on Y-axis rotation. Again the double- and triple-tether configurations perform identically. However, at lower potentials the nodes reach undesirable rotation angles. The lower rotation rates and the large node rotation agrees with Figure 8(b) and shows that for a two-node TCS configuration the Y-axis has the least rotational stiffness.

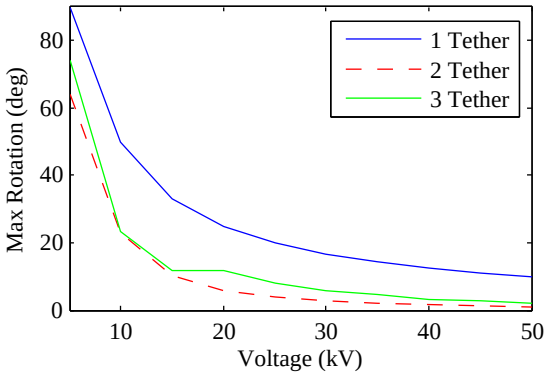

a) Case 1: X-axis rotation

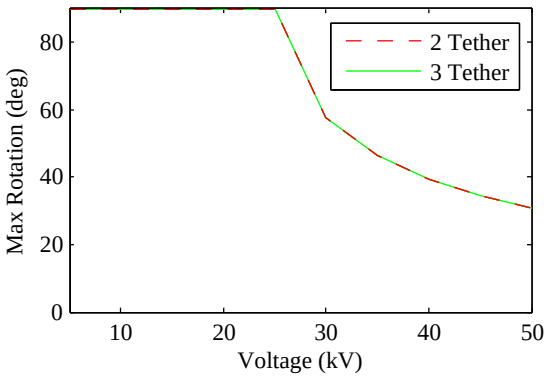

b) Case 2: Y-axis rotation

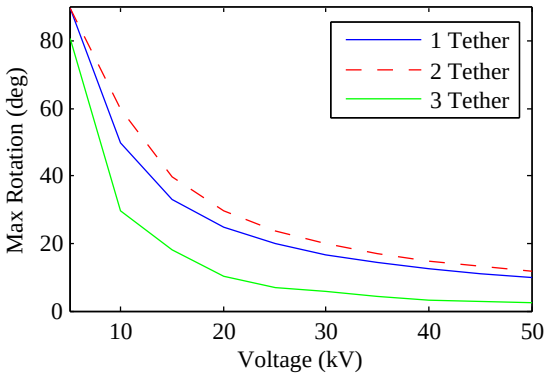

c) Case 3: Z-axis rotation

Figure 10: Maximum absolute principal rotation as a function of nodal potential

Case 3: For a single-tether the Z-axis rotation is identical to X-axis rotation. However, Figure 8(c) shows that a double-tether configuration provides less stiffness than a single-tether for rotations about the Z-axis. Again the moment arm is the cause for this reduced stiffness. The moment arm about the Z-axis in Figure 5(b) is less than what the moment arm of a single-tether provides. The moment arm for this configuration is only in the Y direction and is reduced proportionally to the attachment angle ϕ. A triple-tether configuration also has a moment arm that is dependent on ϕ but the maximum rotation is less than that of a single-tether. The additional stiffness in a triple-tether configuration is because tethers 2 and 3 in Figure 5(d) provide a larger moment arm about the Z-axis. The larger moment arm arises because tethers 2 and 3 are not located in the ZY plane, which adds additional length to the moment arm.

The relative angular deflection about the Z-axis is shown in Figure 9(c). These results indicate that the double-tether system will reach entanglement at disturbances above 22.5 deg/min. The triple-tether however performs significantly better than than the double- and single-tether configurations at keeping the node away from entanglement.

The rotational stiffness for rotations about the Z-axis and dependance on node potential is shown in Figure 10(c). The figure shows that a triple-tether configuration provides more rotational stiffness than a single-tether. Also, a double-tether configuration again provides lower stiffness than a single-tether for rotations about the Z-axis.

Case Summary: The results of Figure 8 indicate that there is up to a 75% decrease in the absolute maximum angular rotation about the X-axis by using a triple-tether over a single-tether. Similarly, there is up to a 60% decrease in the Z-axis rotation with a triple-tether over the single. As the single-tether offers no Y-axis rotational stiffness the addition of tethers does provide rotational stiffness. These values are approximate and are calculated for an initial rotation rate of 20 deg/min and a node voltage of 30 kV. The actual quantitative increase in stiffness is a function of the initial rotation rate and node potential.

The multiple tether configurations have a geometry that places the tether attachment point closer to the entanglement rotation prior to any rotational motion. The results of Figure 9 indicate that the multiple tethers offer minimal advantage in reducing the chances of entanglement, and sometimes perform worse than a single-tether. The advantage of using multiple tethers is that it reduces the absolute nodal rotation for an equivalent initial disturbance as well as introducing 3D rotational stiffness.

In addition, these results suggest that an equally spaced quad tether might offer all axis rotational stiffness as well as symmetric moment arms. This combination may provide an advantageous rotational stiffness capability over the tether configurations used in this study. However, a quad tether configuration is no longer statically determinate and to not develop further mathematical and application assumptions in order to solve, this case will not be investigated here.

D. Spacecraft Nodal Properties

To further expand the TCS capabilities it is advantageous to explore other system parameters that affect the rotational stiffness of the system. Spacecraft nodal parameters such as radius, mass distribution and tether attachment angle are critical components in determining the rotational stiffness of a TCS configuration. Figure 11 shows the effect of varying these nodal parameters on the maximum absolute rotation of a two-node configuration, disturbed about the X-axis.

Figures 11(a) and 11(b) show the results for a single-tether TCS as a function of mass distribution and nodal radii respectively. Similar trends can be shown for multiple tether configurations. The results of multiple tethers are shifted in maximum angle in the same ratio as the comparison shown in Figure 8(a). Figure 11(c) shows the results of a double-and triple-tether TCS configuration as a function of the tether attachment angle ϕ. All other simulation parameters are listed in Table 1.

With a node of a certain mass and radius, the shell model provides the largest possible nodal inertia. This scenario then shows the lower bound on the rotational stiffness that can be achieved. The solid sphere (homogeneous mass distribution throughout the sphere) will have a lower inertia, and thus increased rotational stiffness. However, even the solid sphere model is very conservative. Ideally the TCS nodes would have most of their mass near the node center, and thus obtain an even lower moment of inertia. As Figure 11(a) indicates, compared to the shell model, a 2-3 fold increase in the rotational stiffness can be achieved by designing the TCS nodes to have their most massive components near the nodal center, and thus a lower inertia. Additionally, for a constant mass distribution, solid sphere, Figure 11(b) shows that larger node radii increase the rotational stiffness. Even though the inertia is increasing for larger radii, the larger moment arms for the tethers dominates and thus increases the stiffness. Therefore, Figures 11(b) and 11(c) indicate that the ideal TCS would have its attachment points the furthest away from the center of the craft. Additionally, Figure 11(c) shows that as the tether attachment angle increases (moment arm increases) the maximum absolute rotation

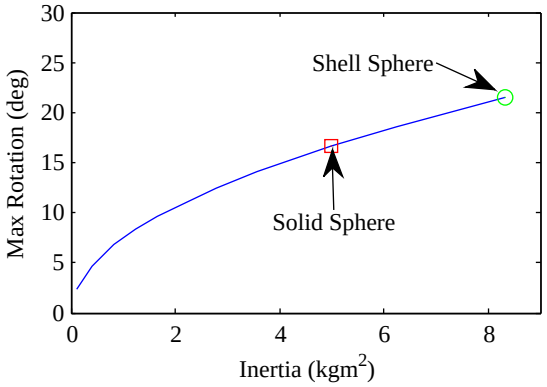

a) Variation in nodal mass moment of inertia

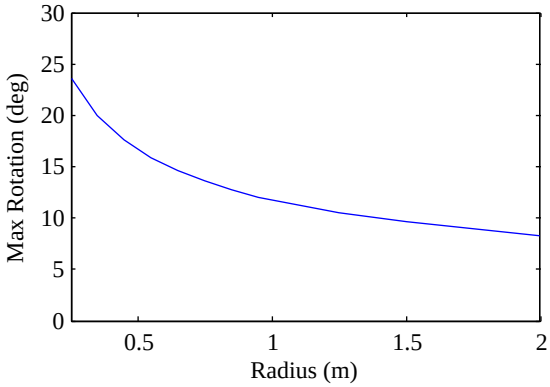

b) Variation in node radius

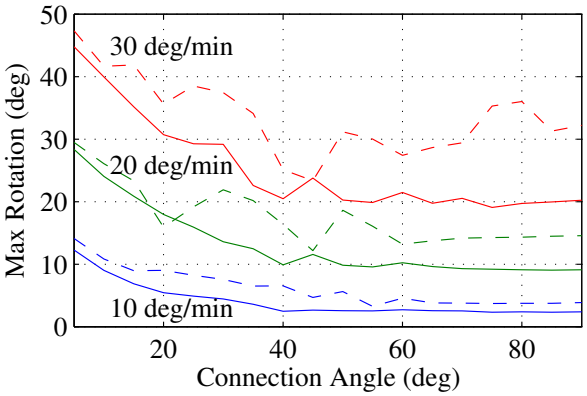

c) Variation in tether attachment angle (Solid: double-tether, Dashed: triple-tether)

Figure 11: Maximum principal rotation as a function of nodal parameters

decreases. Based on the results of this figure an ideal tether attachment angle is approximately 45 degrees. A larger angle (ϕ) offers minimal decrease in absolute angular deflection while placing the node closer to the tether entanglement rotation, as defined in Table 2.

E. Conceptual Node Design

Taking into consideration the results of the previous section an ideal TCS spacecraft node design may appear similar to the conceptual illustration of Figure 12. This design maximizes the spacecraft rotational stiffness, increases nodal wrap-up angles and provides a spherical conductive surface for even Coulomb force generation. The mass moment of inertia is minimized by placing the spacecraft components within a low-mass exterior conducting shell. The tethers are connected to attachment arms that extend beyond the shell increasing the tether moment arms and consequently rotational stiffness. This attachment arm design also increases the maximum angle before nodal wrap up.

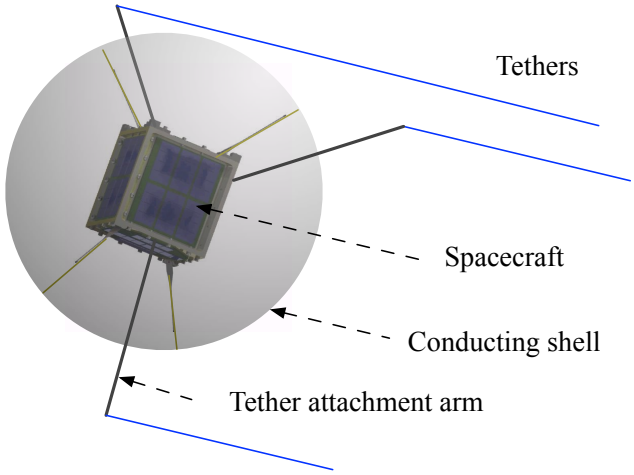

Figure 12: Illustration of conceptual TCS spacecraft node design

IV. Space Plasma Environmental Impacts

Another important component of the TCS feasibility study is the consideration of spacecraft and plasma interactions. The dynamic motion of the TCS system is affected by the plasma, shielding the effective charge and consequently repulsive force between nodes. The plasma will also bombard the spacecraft resulting in a net current flow that will drive the craft to a floating potential. In order to control the potential of the craft, a charge emission device is required to aid or overcome this plasma current. A measure of the shielding influence on rotational stiffness as well as a power budget for counteracting the plasma current is computed.

A. GEO Space Environment Overview

The effective shielding and plasma current is a function of the vehicle potential as well as the plasma environment itself. In order to quantify the extent of force shielding and net current flow, it is necessary to have a representative model of the GEO plasma environment. Although offering simple insight, it is difficult to model the GEO environment with nominal density and velocity values (Maxwellian distribution) as the plasma conditions vary greatly and have a wide variety of energy ranges.[33] The GEO plasma environment can also rapidly fluctuate and can be flooded with high energy particles, with mean values as high as a few tens of keV. The local plasma conditions are heavily dependent on the time as well as the geomagnetic activity which is driven by solar activity.[34]

Three representative GEO plasma conditions are used for this TCS analysis (quiet, nominal, and disturbed). Although single Maxwellian distributions are used, these three plasma conditions define the extreme bounds and nominal operating regimes TCS spacecraft will encounter on-orbit. The single Maxwellian parameters used to describe each of these GEO environments along with the corresponding Debye lengths are shown in Table 4. These GEO plasma values are based on data from the ATS-5 and ATS-6 spacecraft interpreted by References 35 and 36 respectively. It is assumed that the GEO plasma contains a singly ionized species (H^+) that is in thermal and charge equilibrium with the electrons.

Table 4: Representative GEO Single Maxwellian Plasma Parameters and Debye Lengths

Conditions	T_e [keV]	n_e [cm^{-3}]	T_i [keV]	n_i [cm^{-3}]	λ_D [m]
Quiet	0.003	10	0.003	10	**4**
Nominal	0.9	1.25	0.9	1.25	**200**
Disturbed	10	1	10	1	**743**

The quiet plasma (λ_D = 4 m) bounds the 'worst-case' conditions an operating TCS mission could encounter at GEO. This quiet plasma will result in the upper power limit and is also most detrimental due to shielding of the Coulomb force. The worst case parameters are only characteristic as no data of a single Maxwellian with values to this extent have been found. Nominal plasma conditions are a closer representation of the typical operating conditions at GEO, while a disturbed environment is the lower limit of power requirements and shielding.

B. Plasma Shielding Impact on Rotational Stiffness

Analyzed here is the effect of charge shielding which reduces the inflationary Coulomb force and stiffness capabilities of the system.[23] The charge reduction is examined for a range of Debye lengths from nominal to worst-case conditions. Figure 13 shows the effect of these plasma conditions on the rotational stiffness of a single-tether TCS configuration with disturbance about the X-axis. The results shown are for the conservative partial charge shielding force model of Eq. (4). A spacecraft charging to these potentials will result in a larger effective debye length and in fact improve these rotational stiffness results.

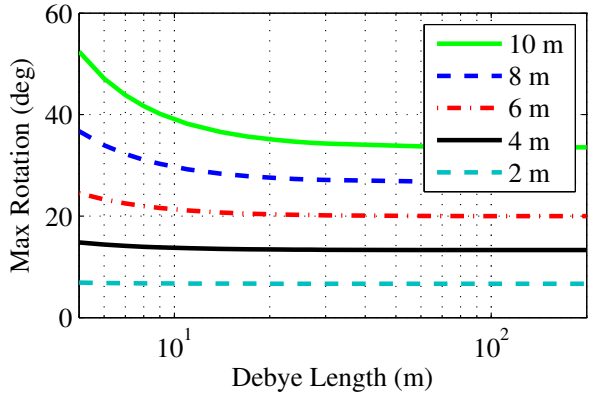

a) Variation in nodal separation

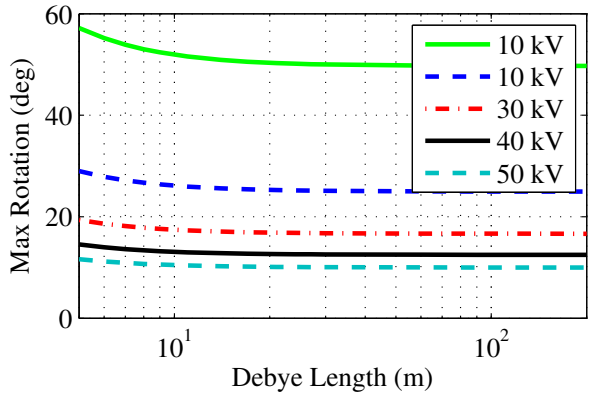

b) Variation in nodal potential

Figure 13: Maximum absolute principal rotation as a function of plasma conditions (Debye length)

Figure 13 shows that environmental conditions have minimal impact on the dynamics of a closely-operated TCS system until Debye lengths on the order of 10 meters or smaller are considered. Nominal values of Debye lengths (far right of figure) have no effect, but as the plasma Debye length reduces to the worst case value the rotational stiffness decreases. The maximum absolute rotation lines in the figures converge to the maximum rotation values with no plasma shielding. When designing for the worst case plasma conditions consideration must be made for TCS nodal separations larger than 5 meters. Considering a TCS system with a large number of nodes spanning 100 meters, the shorter Debye length plasma shielding will also impact the overall rigidity of this system. The results in Figure 13 are specific to a simple two-node system and short separations.

C. Power Requirements to Maintain a Fixed Potential in a Plasma

The TCS plasma environment shields the Coulomb force between nodes but also results in a net current (I_{net}) to the craft. The net current is computed for a single TCS node in each of the three plasma conditions and used to compute the power necessary to maintain a fixed potential. It is assumed that the charge control current (I_{cc}) can be either positive or negative charge and equal the net plasma current $I_{\text{net}} = I_{cc}$.

The current flow between spacecraft and its local plasma is computed for a node of radius 0.25 m. It is assumed the plasma is comprised of two populations (electrons, protons) that are modeled with single Maxwellian distributions. A spacecraft at GEO is stationary relative to the plasma and the two primary current contributions are from electron and ion bombardment. The net current density J_{net}, is developed for both positive and negatively charged spacecraft with the notation that all currents to the spacecraft are negative:[34,37,38]

$$J_{\text{net}}(V_{sc} < 0) = J_{0e} \exp\left[\frac{-e_c|V_{sc}|}{\kappa T_e}\right] - J_{0i}\left(1 + \frac{e_c|V_{sc}|}{\kappa T_i}\right) \tag{5a}$$

$$J_{\text{net}}(V_{sc} > 0) = J_{0e}\left(1 + \frac{e_c V_{sc}}{\kappa T_e}\right) - J_{0i} \exp\left[\frac{-e_c V_{sc}}{\kappa T_i}\right] \tag{5b}$$

where J_{0e} and J_{0i} are the electron and ion saturation currents:

$$J_{0e} = e_c n_e \sqrt{\frac{\kappa T_e}{2\pi m_e}} \tag{6a}$$

$$J_{0i} = e_c n_i \sqrt{\frac{\kappa T_i}{2\pi m_i}} \tag{6b}$$

A spacecraft will reach current equilibrium with the plasma when $J_{\text{net}} = 0$. Depending on the plasma conditions this solution exists for a specified spacecraft floating potential. With a single Maxwellian plasma distribution and no photoelectron or secondary particle effects the equilibrium will occur at a negative potential. It is important to include the effects of photoelectrons as they can be a dominant current and a GEO spacecraft spends the majority of its orbit in sunlight. The photoelectron current is added to the net current of Equations 5 with the expressions:

$$J_{pe}(V_{sc} < 0) = -J_{0pe} \tag{7a}$$

$$J_{pe}(V_{sc} > 0) = -J_{0pe} \exp\left[\frac{-e_c V_{sc}}{\kappa T_{pe}}\right]\left(1 + \frac{e_c V_{sc}}{\kappa T_{pe}}\right) \tag{7b}$$

where J_{0pe} is the constant photoelectron current density for a spacecraft and T_{pe} is the mean energy of the photoelectrons leaving the spacecraft surface. The photoelectron current is dependent on the surface materials of the spacecraft. For this study a photoelectron current of $J_{0pe} = 20\ \mu\text{Am}^{-2}$ will be used along with a mean energy $T_{pe} = 2$ eV.[11,31,37,39,40] These values are chosen to represent typical spacecraft materials and give a conservative indication of the effect of photoelectron currents on TCS power requirements. The photoelectron current is computed from only the sun-lit surface (half-sphere).

Additional current sources that are not included in the model are the outgoing electrons from secondary emissions and backscattering.[41] The secondary yield (that can be higher than the incoming primary particle flux)[42] is a function of the surface material and the primary particle energy. The mean energy of the secondary electron leaving the surface is very low, $T_{\text{Se}} \approx$ 2-3 eV[34,43,44] and will return to the surface of a positively charge craft (no net current effect).

For a highly negatively charge craft, the electron current is low so the secondary electron and backscattered current from electron impacts is omitted. The backscattering of ions is generally very

low and is also omitted.[34,45] The secondary electron yield is considerable only for ion impacts with high primary energies ($>$ 10 keV)[34] and should be considered for the higher energy plasmas of the nominal and disturbed conditions. This however can also be omitted in these plasma conditions as the dominant current (by at least an order of magnitude) is the photoelectrons.

The net current is modeled over a range of feasible spacecraft operating potentials and the corresponding power is calculated using $P = |V_{sc} I_{\text{net}}|$. For a spacecraft in eclipse (no photoelectrons) the power required to maintain a fixed potential is shown in Figure 14(a) for each plasma condition. The nominal (λ_D = 200 m) and disturbed plasma conditions require achievable Watt-levels of power, while the quiet plasma power is still feasible with a worst case maximum value of 100 W.

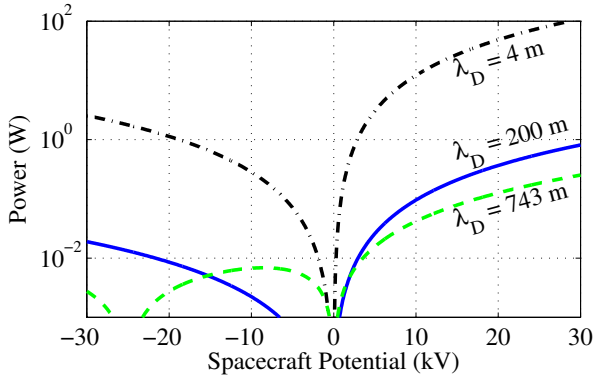

a) Operating in eclipse

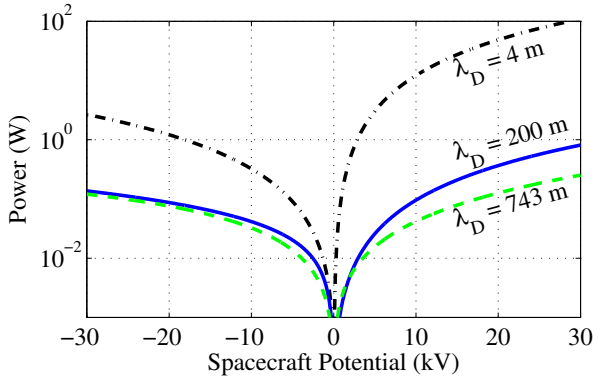

b) Operating in sun light

Figure 14: Power required to maintain fixed spacecraft potential for each plasma condition

For a spacecraft in sun light the power required to maintain a fixed potential is shown in Figure 14(b) for each plasma condition. The inclusion of photoelectrons has very little effect on the power for a quiet plasma (λ_D = 4 m). The inclusion of photoelectrons for negative potentials in nominal and disturbed plasmas slightly raises the required power. However, the values are still an order of magnitude lower than the quiet plasma.

In Figure 14(a) the low power dip in the disturbed plasma (λ_D = 743 m) occurs at -25 kV where the bombardment of high temperature electrons equals the attracted ion current. The nominal and quiet plasmas also have equilibrium conditions, but at further negative spacecraft potentials.

The results of Figure 14 showing the required power to maintain a desired potential in a nominal GEO plasma can be practically achieved with current technology.[46] Even for a worst case plasma condition the power requirement increases to only 3W to charge a node to -30 kV. The results also show that there are power saving advantages by charging to negative potentials across all plasma conditions. Negative charging is achieved by emitting ions through hollow cathode or field evaporation emission.

V. Conclusion

This study analyzes the rotational dynamics of a two-node TCS system interconnected through 1-3 tethers. Full 3D simulations provide insight into how well the TCS is able to reject initial angular rate disturbances and avoid tether/node interaction issues. The study is performed for a single-, double- and triple-tether configuration. Additional tethers increase the rotational stiffness, while reducing the resulting absolute angular node deflection by up to 75%. While the absolute maximum rotation is reduced with multiple tethers, the nodes are still susceptible to entanglement as the tether attachment points are initially closer to the maximum rotation angle. With a triple-tether configuration rotational control is achieved about all axis. Future simulations could incorporate system damping that would assist with rotational disturbance rejection. This study indicates that a TCS system can be stiffened under Coulomb forces to resist deployment or external rotational disturbances on the order of 30-60 degrees per minute. While these are small rotational rates, they provide an indication of how smoothly the TCS nodes must be separated and deployed if no controls or damping are considered.

With the development of the TCS concept it is beneficial to understand the effect of nodal inertia, radial size, and tether attachment angle (for multiple tethers) on the rotational stiffness. The advantages of a lower inertia are quantified along with the increased moment arm from larger node sizes. Two- to three-fold increases in rotational stiffness can be achieved by moving the node mass towards its center. Larger nodes have to consider space plasma interaction and power requirements which are also modeled in this study. Using representative GEO plasmas it is shown that Coulomb force shielding is minimal in a nominal environment. In addition, it is demonstrated that the power levels required to maintain a fixed potential using a charge emission device are feasible with current space proven technology. The prospects of the TCS concept are strengthened with these findings and will lead to further development.

Acknowledgments

We would like to thank Dr. Daniel F. Moorer in his assistance in determining representative space weather parameters to be considered. We would also like to acknowledge the government support to conduct this study.

Appendix

Additional Appendix Nomenclature

$[\mathcal{BI}]$	=	direction cosine matrix from inertial to body frame
$\mathbf{\Gamma}_i$	=	total body torque
$[I]$	=	mass moment of inertia matrix
$[I_{3x3}]$	=	identity matrix
k	=	tether index number
$[K]$	=	node adjacency matrix
K_{ij}	=	ij^{th} scalar value from adjacency matrix
δL_{ijk}	=	change in length of tether k
M	=	number of tethers between two-nodes
μ	=	gravitational coefficient for Earth
N	=	total number of nodes
$\dot{\boldsymbol{\omega}}_i$	=	angular acceleration
$\boldsymbol{\omega}_i$	=	angular velocity
$\boldsymbol{p}_{ijk}$	=	tether attachment point
$\ddot{\boldsymbol{R}}_i$	=	inertial acceleration vector of node
$\hat{R}_i$	=	inertial unit vector of node position
$\boldsymbol{\sigma}_i$	=	modified Rodrigues parameter
$\dot{\boldsymbol{\sigma}}_i$	=	modified Rodrigues parameter rate
$[\tilde{\boldsymbol{\sigma}}]$	=	skew symmetric matrix of $\boldsymbol{\sigma}$
$\boldsymbol{T}_{ij}$	=	total tensile force between nodes i and j
$\boldsymbol{\tau}_{ijk}$	=	unit vector for tether k between nodes i and j

The adjacency matrix, $[K_{ij}]$, defines which nodes are connected and by how many tethers. The tether length increase of tether k between nodes i and j is defined by δL_{ijk}. The resulting tensile

force acting on node i from the tether(s) connected to node j is:

$$\boldsymbol{T}_{ij} = k_{\mathrm{s}} \sum_{k=1}^{M} \delta L_{ijk} \hat{\boldsymbol{\tau}}_{ijk} \tag{8}$$

where M is the number of tethers between nodes i and j as defined by $[K_{ij}]$ and $\boldsymbol{\tau}_{ij}$ is the vector defining the k^{th} tether's connections between node i to j.

A. Translational Equation of Motion

Using the Coulomb force of Equation (4) and tensile force, the resulting equations of motion of each node is calculated using:

$$\begin{aligned} \ddot{\boldsymbol{R}}_i &= -\frac{\mu}{|\boldsymbol{R}_i|^2}\hat{R}_i \\ &+\sum_{j=1}^{N} K_{ij}\frac{\boldsymbol{T}_{ij}}{m_i} + \sum_{j=1}^{N} \frac{k_c q_i q_j (-\hat{\boldsymbol{r}}_{ij})}{m_i r_{ij}^2} e^{-r_{ij}/\lambda_D}\left(1+\frac{r_{ij}}{\lambda_D}\right) \ , \ i \neq j \end{aligned} \tag{9}$$

where $\mu = 3.986 \times 10^{14}$ m^{3}s^{-2} is the gravitational coefficient for Earth, m_i is the spacecraft node mass, N is the total number of nodes in the TCS model, and K_{ij} is a scalar based on the adjacency matrix which is 0 if no tethers connected or 1 if any tethers are connected. Note that these charges do not influence the inertial motion of the TCS center of mass. They simply provide an inflating force, relative to the systems center of mass, that increases the tether tensions. In addition, the Coulomb force is calculated based on a point charge approximation, even though the nodes have a distributed surface charge. The motion of each node is propagated in time using a variable step Runge-Kutta algorithm. A external disturbance force is added as an inertial vector to Equation (9).

B. Rotational Equation of Motion

The attitude of each spacecraft node is also propagated by computing the torque acting on the node from each tether:

$${}^{\mathcal{B}}\boldsymbol{\Gamma}_i = \sum_{j=1}^{N}\left[\sum_{k=1}^{M}\left(K_{ij}\,{}^{\mathcal{B}}\boldsymbol{p}_{ijk} \times [\mathcal{BI}]_i\,{}^{\mathcal{I}}\boldsymbol{T}_{ijk}\right)\right] \ , \ i \neq j \tag{10}$$

Where $\boldsymbol{p}_{ijk}$ is the body fixed vector that defines the location of the k^{th} tether attachment point on node i that connects to node j and $[\mathcal{BI}]_i$ is the direction cosine matrix of the attitude of node i relative to the inertial frame. The angular acceleration of each node is defined in the body frame with Euler's rotational equations of motion:[47]

$$[I]\dot{\boldsymbol{\omega}}_i = -\boldsymbol{\omega}_i \times ([I]\boldsymbol{\omega}_i) + \boldsymbol{\Gamma}_i \tag{11}$$

The attitude of each node is represented with the modified rodrigues parameters (MRP) which are integrated using the differential kinematic equation:

$$\dot{\boldsymbol{\sigma}}_i = \frac{1}{4}\left[(1-\sigma_i^2)[I_{3x3}] + 2[\tilde{\boldsymbol{\sigma}}]_i + 2\boldsymbol{\sigma}_i\boldsymbol{\sigma}_i^T\right]\boldsymbol{\omega}_i \tag{12}$$

The MRP set will go singular with a rotation of $\pm 360^\circ$. To ensure a non-singular description, the MRP description is switched to the shadow set whenever $|\boldsymbol{\sigma}| > 1$.[47]

References

[1] Freeland, R. E., Bilyeu, G. D., , Veal, G. R., and Mikulas, M. M., "Inflatable Deployable Space Structures Technology Summary," *49th International Astronautical Congress*, Melbourne, Australia, Sept. 28 – Oct. 2 1998.

[2] Cobb, R. G., Lindemuth, S. N., Slater, J. C., and Maddux, M. R., "Development and Test of a Rigidizable Inflatable Structure Experiment," *45th AIAA/ASME/ASCE/AHS/ASC Structures, Structural Dynamics & Materials Conference*, Palm Springs, CA, April 19–22 2004, Paper No. AIAA 2004–1666.

[3] Tarazaga, P. A., Inman, D. J., and Wilkie, W. K., "Control of a Space Rigidizable Inflatable Boom Using Macro-fiber Composite Actuators," *Journal of Vibration and Control*, Vol. 13, No. 7, 2007, pp. 935–950.

[4] Fang, H., Knarr, K., Quijano, U., Huang, J., and Thomson, M., "In-space Deployable Reflectarray Antenna: Current and Future," *AIAA/ASME/ASCE/AHS/ASC Structures, Structural Dynamics and Materials Conference*, Schaumburg, IL, April 7-10 2008, Paper No. AIAA 2008-2209.

[5] Hyde, R., Dixit, S., Weisberg, A., and Rushford, M., "Eyeglass: A Very Large Aperture Diffractive Space Telescope," *SPIE – Highly Innovative Space Telescope Concepts*, Vol. 4849, Dec. 18 2002, pp. 28–39.

[6] Hyde, R., "Eyeglass Large Aperture, Lightweight Space Optics," Tech. Rep. UCRL-ID-151390, University of California, Lawrence Livermore National Laboratory, Feb. 10 2003.

[7] Carpenter, K. G., Schrijver, C. J., Karovska, M., and Team, S. M. C. D., "The Stellar Imager (SI) Project: A Deep Space UV/Optical Interferometer (UVOI) to Observe the Universe at 0.1 Milli-arcsec Angular Resolution," *Astrophysics and Space Science*, Vol. 320, No. 1-3, April 2009, pp. 217–223.

[8] Blackwood, G., Henry, C., Serabyn, E., Dubovitsky, S., Aung, M., and Gunter, S. M., "Technology and Design of an Infrared Interferometer for the Terrestrial Planet Finder," *AIAA Space 2003*, Long Beach, CA, Sept. 23–25 2003, Paper No. AIAA 2003-6329.

[9] Brown, O. and Eremenko, P., "Fractionated Space Architectures: A Vision for Responsive Space," *4th Responsive Space Conference*, Los Angeles, CA, April 23–26 2006, Paper No. AIAA-RS-2006-1002.

[10] Gill, E., D'Amico, S., and Montenbruck, O., "Autonomous Formation Flying for the PRISMA mission," *AIAA Journal of Spacecraft and Rockets*, Vol. 44, No. 3, May–June 2007, pp. 671–681.

[11] King, L. B., Parker, G. G., Deshmukh, S., and Chong, J.-H., "Spacecraft Formation-Flying using Inter-Vehicle Coulomb Forces," Tech. rep., NASA Institute for Advanced Concepts (NIAC), January 2002.

[12] Schaub, H., Parker, G. G., and King, L. B., "Challenges and Prospect of Coulomb Formations," *Journal of the Astronautical Sciences*, Vol. 52, No. 1–2, Jan.– June 2004, pp. 169–193.

[13] Miller, D. W., , Sedwick, R. J., Kong, E. M. C., and Schweighart, S., "Electromagnetic Formation Flight for Sparse Aperture Telescopes," *IEEE Aerospace Conference Proceedings*, Vol. 2, Big Sky, Montana, March 9–16 2002, pp. 2–729 – 2–741.

[14] Peck, M. A., Streetman, B., Saaj, C. M., and Lappas, V., "Spacecraft Formation Flying using Lorentz Forces," *Journal of British Interplanetary Society*, Vol. 60, July 2007, pp. 263–267.

[15] Gersh, J., "Architecting the Very-Large-Aperture Flux-Pinned Space Telescope: A Scalable, Modular Obtical Array with High Agility and Passively Stable Orbital Dynamics," *AAS/AIAA Astrodynamics Specialist Conference*, Honolulu, Hawaii, Aug. 18–21 2008, Paper No. AIAA 2008-7212.

[16] Schaub, H., Parker, G. G., and King, L. B., "Coulomb Thrusting Application Study," Tech. rep., Virginia Tech and Aerophysics, Jan. 2006.

[17] Natarajan, A. and Schaub, H., "Linear Dynamics and Stability Analysis of a Coulomb Tether Formation," *AIAA Journal of Guidance, Control, and Dynamics*, Vol. 29, No. 4, July–Aug. 2006, pp. 831–839.

[18] Natarajan, A. and Schaub, H., "Orbit-Nadir Aligned Coulomb Tether Reconfiguration Analysis," *AAS/AIAA Spaceflight Mechanics Meeting*, Galveston, TX, Jan. 27–31 2008, Paper AAS 08–149.

[19] Natarajan, A., Schaub, H., and Parker, G. G., "Reconfiguration of a Nadir-Pointing 2-Craft Coulomb Tether," *Journal of British Interplanetary Society*, Vol. 60, No. 6, June 2007, pp. 209–218.

[20] Wang, S. and Schaub, H., "Switched Lyapunov Function Based Coulomb Control of a Triangular 3-Vehicle Cluster," *AAS/AIAA Astrodynamics Specialist Conference*, Pittsburgh, PA, Aug. 9–13 2009, Paper No. AAS 09–391.

[21] Izzo, D. and Pettazzi, L., "Self-assembly of large structures in space using intersatellite Coulomb forces," *57th International Astronautical Congress*, Valencia, Spain, October 2006, Paper IAC-06-C3.4/D3.4.07.

[22] Seubert, C. R. and Schaub, H., "Tethered Coulomb Structures: Prospects and Challenges," *AAS F. Landis Markley Astrodynamics Symposium*, Cambridge, MA, June 30 – July 2 2008, Paper No. AAS 08–269.

[23] Seubert, C. R. and Schaub, H., "Impact of Nodal Attitude Motion on Two-Element Tethered Coulomb Structures," *AAS/AIAA Spaceflight Mechanics Meeting*, San Diego, CA, Feb. 14-17 2010, Paper No. AAS 10–268.

[24] Mullen, E., Frederickson, A. R., Murphy, G. P., Ray, K. P., Holeman, E. G., Delorey, D., Robson, R., and Farar, M., "An Autonomous Charge Control System at Geosynchronous Altitude: Flight Results for Spacecraft Design Considerations," *IEEE Transactions on Nuclear Science*, Vol. 44, No. 6, December 1997, pp. 2188 – 2914.

[25] Fennell, J. F., Koons, H. C., Roeder, J. L., and Blake, J. B., "Spacecraft Charging: Observations and Relationship to Satellite Anomalies," *Proceedings of 7th Spacecraft Charging Technology Conference*, ESA Spec. Publ., Noordwijk, The Netherlands, April 23–27 2001, pp. 279–285.

[26] Garrett, H. B. and Whittlesey, A. C., "Spacecraft Charging, An Update," *IEEE Transactions on Plasma Science*, Vol. 28, No. 6, Dec. 2000, pp. 2017–2028.

[27] Torkar, K., Riedler, W., Rudenauer, F., Escoubet, C. P., Arends, H., Narheim, B. T., Svenes, K., McCarthy, M. P., Parks, G. K., Lin, R. P., and Reme, H., "Spacecraft Potential Control aboard Equator-S as a Test for Cluster-II," *Annales Geophysicae*, Vol. 17, No. 12, 1999, pp. 1582–1591.

[28] Torkar, K., Riedler, W., Escoubet, C. P., Fehringer, M., Schmidt, R., L., G. R. J., Arends, H., Rudenauer, F., Steiger, W., Narheim, B. T., Svenes, K., Torbert, R., M., A., Fazakerley, A., Goldstein, R., Olsen, R. C., Pedersen, A., Whipple, E., and Zhao, H., "Active Spacecraft Potential Control for Cluster – Implementation and First Results," *Annales Geophysicae*, Vol. 19, No. 10/12, 2001, pp. 1289–1302.

[29] Pisacane, V. L., *The Space Environment and its Effects on Space Systems*, AIAA Education Series, Reston, VA, 2008, Pages 208–209.

[30] Gurnett, D. A. and A., B., *Introduction to Plasma Physics - with Space and Laboratory Applications*, Cambridge University Press, New York, NY, 2005, Pages 8–9.

[31] Whipple, E. C., "Potentials of surfaces in space," *Reports on Progress in Physics*, Vol. 44, No. 11, 1981, pp. 1197–1250.

[32]Murdoch, N., Izzo, D., Bombardelli, C., Carnelli, I., Hilgers, A., and Rodgers, D., "Electrostatic Tractor for Near Earth Object Deflection," *59th International Astronautical Congress*, Glasgow, Scotland, 2008, Paper IAC-08-A3.I.5.

[33]DeForest, S. E., "The Plasma Environment at Geosynchronous Orbit," *1st Spacecraft Charging Technology Conference*, 1977.

[34]Hastings, D. E. and Garrett, H. B., *Spacecraft-Environment Interactions*, Cambridge University Press, 1996, pp. 142–180.

[35]Garrett, H. B. and DeForest, S. E., "An Analytical Simulation of the Geosynchronous Plasma Environment," *Planetary Space Science*, Vol. 27, 1979, pp. 1101–1109.

[36]Lennartsson, W. and Reasoner, D. L., "Low-Energy Plasma Observations at Synchronous Orbit," *Journal of Geophysical Research*, Vol. 83, No. A5, 1978, pp. 2145 – 2156.

[37]Lai, S. T. and Tautz, M., "High-Level Spacecraft Charging at Geosynchronous Altitudes: A Statistical Study," *8th Spacecraft Charging Technology Conference*, Oct. 2003.

[38]Riedler, W., Torkar, K., Rudenauer, F., Fehringer, M., Pedersen, A., Schmidt, R., Grard, R. J. L., Arends, H., Narheim, B. T., Troim, J., Torbert, R., Olsen, R. C., Whipple, E., Goldstein, R., Valavanoglou, N., and Zhao, H., "Active Spacecraft Potential Control," *Space Science Reviews*, Vol. 79, Jan. 1997, pp. 271–302.

[39]Grard, R., "Properties of the Satellite Photoelectron Sheath Derived from Photoemission Laboratroy Measurements," *Journal of Geophysical Research*, Vol. 78, No. 16, 1973, pp. 2885–2906.

[40]Grard, R., Knott, K., and Pedersen, "Spacecraft Charging Effects," *Space Science Reviews*, Vol. 34, 1983, pp. 289–304.

[41]Whipple, E. C., "Observation of Photoelectrons and Secondary Electrons Reflected from a Potential Barrier in the Vicinity of ATS 6," *Journal of Geophysical Research*, Vol. 81, No. 4, Feb. 1976, pp. 715–719.

[42]Lai, S. T., "The Importance of Surface Conditions for Spacecraft Charging," *AIAA Aerospace Sciences Meeting*, Orlando, FL, Jan. 5 – 8 2009, Paper AIAA 2009-349.

[43]Francis, C. R., "Electrostatic Charging Problems of Spacecraft," *Journal of Electrostatics*, Vol. 11, 1982, pp. 265–280.

[44]Prokopenko, S. M. L. and Laframboise, J. G., "High-Voltage Differential Charging of Geostationary Spacecraft," *Journal of Geophysical Research*, Vol. 85, No. A8, Aug. 1980, pp. 4125–4131.

[45]DeForest, S. E., "Spacecraft Charging at Synchronous Orbit," *Journal of Geophysical Research*, Vol. 77, No. 4, Feb. 1972, pp. 651–659.

[46]Torkar, K., Fazakerley, A., and Steiger, W., "Active Spacecraft Potential Control: Results from the Double Star Project," *IEEE Transactions on Plasma Science*, Vol. 34, No. 5, Oct. 2006, pp. 2046–2052.

[47]Schaub, H. and Junkins, J. L., *Analytical Mechanics of Space Systems*, AIAA Education Series, Reston, VA, 2nd ed., October 2009.